Redox Oxide@Molten Salt as a generalized catalyst design strategy for oxidative dehydrogenation of ethane via selective hydrogen combustion

Junchen Liu^{l‡}, Seif Yusuf^{l‡}, Daniel Jackson^l, William Martin^l, Dennis Chacko^l, Kyle Vogt-Lowell^l, Luke Neal^{l*}, Fanxing Li^{l*}

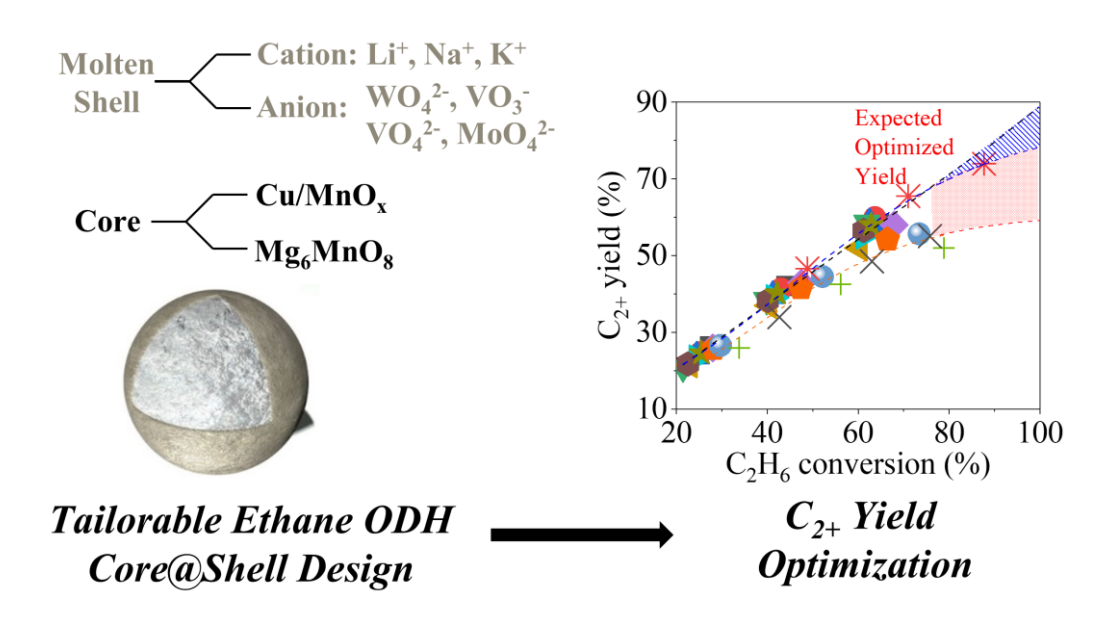
1 Department of Chemical and Biomolecular Engineering, North Carolina State University,
Raleigh, NC, 27606

Abstract

The current study demonstrates a redox oxide @ molten salt core-shell architecture as a generalized redox catalyst design strategy for chemical looping – oxidative dehydrogenation of ethane. 17 combinations of redox active oxides and molten salts were prepared, evaluated, and characterized. X-ray diffraction indicates that the redox oxides and molten salts are fully compatible, forming separate and stable phases. X-ray photoelectron spectroscopy demonstrates that the molten salts aggregate at the redox oxide surface, forming a core-shell structure to block the non-selective sites responsible for CO_x formation. Up to \sim 74% single-pass olefin yields were achieved using the proposed redox catalyst design strategy. Statistical analyses of the performance

^{*} Corresponding Authors: fli5@ncsu.edu, lmneal2@ncsu.edu

data indicate the potential to achieve up to 86.7% single-pass yield by simply optimizing the operating conditions using the redox catalysts reported in this study. Meanwhile, the generalizability of the catalyst design strategy offers exciting opportunities to further optimize the composition and performance of the redox catalysts for ethane ODH under a chemical looping scheme with significantly reduced energy consumption and CO₂ emissions.



Keyword: oxidative dehydrogenation, catalyst design, chemical looping, ethane, ethylene

1. Introduction

Ethylene is an important commodity chemical to produce various important chemical intermediates and products[1]. The surge of the shale gas production in the United States, which contains a substantial amount of ethane (~24 vol. % ethane in Bakken), has significantly increased ethane supply and thus opened up new opportunities for ethane to ethylene production[2–5]. State-of-the-art for ethylene production is based on steam cracking of ethane and other hydrocarbon feedstocks[6,7]. However, due to the high reaction endothermicity (e.g. *Reaction 1*), limited single pass conversion (~60% at 850 °C), significant steam consumption, and complex downstream

separations, the energy demand for this process is very high (~16 GJ/ton C₂H₄ for ethane cracking)[6,8]. The similarity in the boiling points of unconverted ethane and the ethylene product also makes separation challenging. This, coupled with the various byproducts resulting from gas phase cracking reactions, leads to complex and energy-intensive downstream compression and separation operations, accounting for 40~50% of the total energy consumption of the plant. In addition, the cracker furnaces emit substantial amounts of CO₂ and NO_x[6,8]. Therefore, novel approaches for the autothermal or exothermic conversion of ethane to ethylene are highly desirable to eliminate the equilibrium limitation, simplify downstream separations, and reduce the energy consumption and pollutant emissions.

Oxidative dehydrogenation (ODH) represents such an exothermic, non-equilibrium-limited approach (*Reaction 2*) [7,9–11]. Extensive studies have been performed on catalyst design and optimization with the goal of improving the ethane conversion and ethylene productivity. Major families of heterogeneous catalysts investigated include supported NiO (~35-38% ethylene yield)[12–15], V and V/Mo catalysts (23-32% yield)[16–18], La/Sr/Nd and Cl doped La/Sr/Fe oxides (~55% yields)[19,20], Sn doped Pt (~55% yield or higher)[21–24], Mo/V/Te/Nb/O (M1 catalyst, up to 78% yield)[9,25,26], Mg/Dy/Li/Cl/O (~55% yields)[27,28], carbon nanotube and modified boron nitride (up to 50% yield)[29,30]. From a process design standpoint, ethane/O₂ cofeed requires an energy-intensive air separation unit for oxygen production and raises safety concerns[25,26,31]. In terms of catalyst design, selectivity towards unwanted CO₂ and oxygenates (which are difficult to separate) under O₂-rich environment remains a key challenge[7,9,32]. In addition, the long term stability of these catalysts has not been demonstrated.[26]

Reaction 1: $C_2H_6 \leftrightarrow C_2H_4 + H_2$ $\Delta H_{1123K} = +143 \text{ kJ mol}^{-1}$

Reaction 2: $O_2 + C_2H_6 \leftrightarrow C_2H_4 + H_2O$ $\Delta H_{1123K} = -105 \text{ kJ mol}^{-1}$

Chemical looping-ODH (CL-ODH) provides an alternative route to ethane ODH that overcomes these challenges[32–46]. In CL-ODH, an oxide-based redox catalyst acts as an oxygen carrier to convert ethane with oxygen from its crystal lattice (*Reactions 3*), as shown in the *ODH reactor* in **Figure 1a**. The redox catalyst is then reoxidized in air to regenerate its lattice oxygen (*Reactions 4*), as shown in the *regenerator* in **Figure 1a**. As illustrated in *Reactions 3 and 4*, the exothermic nature of the overall reaction (ODH reaction) can facilitate autothermal operations. The reaction cycle enabled by the redox catalyst also prevents the direct mixing of O₂ and ethane and eliminates the need for air separation.

Reaction 3:
$$C_2H_6 + MeO_x(solid)$$

$$\leftrightarrow$$
 C₂H₄ + H₂O + MeO_{x-1}(solid) Δ H₁(oxide dependent)

$$Reaction \ 4: \qquad \mathbf{O_2} + \mathbf{2MeO_{x-1}}(solid) \leftrightarrow \mathbf{2MeO_x}(solid) \qquad \Delta H_2 = -\mathbf{105} - \Delta H_1 \ kJ \ mol^{-1}$$

Commonly encountered oxygen carriers in chemical looping combustion like Fe₂O₃ and CuO tend to be nonselective for ethane ODH and thus lead to CO_x formation. Several reports have demonstrated that CL-ODH of ethane with FeO/MoO, VO_x, and alkali doped LSF can achieve up to ~50% C₂H₄ yield with 90% selectivity[33–35,38,39,44,47,48]. Luongo et al. has recently reported using nitrates as the precursor to uniformly coats the surface with carbonates as the selective hydrogen combustion catalyst, which, combined with MoVNbTeO based catalyst, achieved ~42% C₂H₆ conversion and 91% of C₂H₄ selectivity at 500 °C[39]. Previously, Yusuf et al. and Neal et al. proposed using Na₂WO₄ as a catalyst surface modifier, validating CL-ODH with Mg₆MnO₈@Na₂WO₄ (MGM@Na₂WO₄) as a potentially attractive approach by achieving <8% CO₂ selectivity and ~86.6% ethane conversion [36,37,49]. This work suggested that the Na₂WO₄ promoter may coat the MGM core as a molten shell under the chemical looping reaction conditions, as shown in **Figure 1b**. The molten salt shell decreased the presence of Mn⁴⁺ in the

near-surface region (verified by XPS), inhibited the dissociative adsorption of oxygen, and decreased the rate of oxygen exchange, leading to significantly lower CO₂ selectivity and higher C₂H₄ selectivity than those of unpromoted MGM[36,49]. Despite suppressing CO_x formation, the shell still support facile oxidation of hydrogen from ethane dehydrogenation. As such, ~90% of the H₂ conversion was achieved using MGM@Na₂WO₄. The high H₂ conversion is beneficial to facilitate the autothermal operation, as illustrated by Haribal et al, resulting in up to 82% reduction in CO₂ emission when compared to state-of-the-art cracking processes[8]. In summary, the molten Na₂WO₄-promoted MGM-based CL-ODH can: (i) Circumvent C₂H₆ cracking equilibrium limitation and maintain high ethylene and C₂₊ selectivity; (ii) Facilitate autothermal operation via facile H₂ combustion[49].

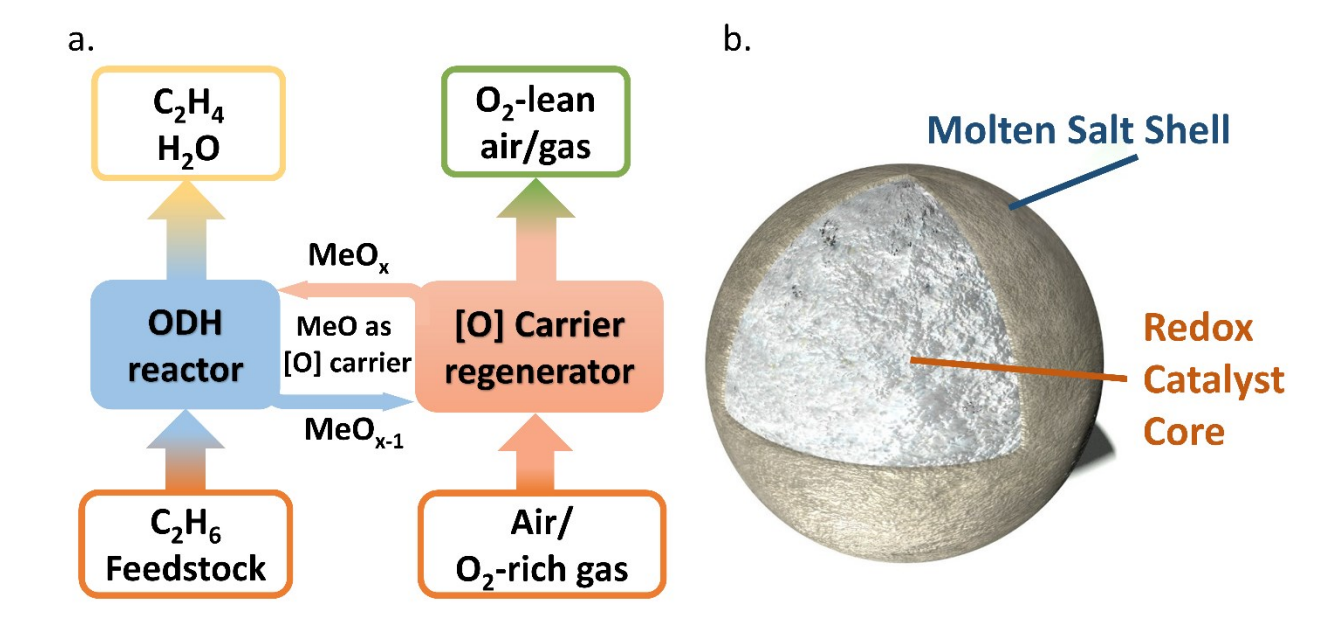


Figure 1. (a) Overall scheme of CL-ODH and (b) schematic illustration of the core-shell structured, molten salt promoted redox catalyst (film thickness is ~8~13 nm and the particle diameter is 425~850 μm)

The current study demonstrates a generalized redox catalyst design strategy, i.e. a redox oxide @ molten salt core-shell architecture, for CL-ODH applications. Specifically, 17 combinations of molten salt promoters (Mo-, V-, and W-containing alkali molten salt and their mixtures) and oxides (CuMn₂O₄ (CMO) and Mg₆MnO₈ (MGM)) were experimentally tested and characterized, confirming the generality of the core-shell structure and its effectiveness for ethane CL-ODH. Up to \sim 74% single pass olefin yields and 85% H₂ conversions at 80 mol. % C₂H₆ feed. The extensive experimental results and the composition-performance relationships will enable further optimization of the redox catalyst for increased ethylene and C₂₊ olefin selectivity and yield under the autothermal CL-ODH scheme with near an order of magnitude lower CO₂ emissions.

2. Experimental Methods

2.1 Redox catalyst synthesis

Table 1 summarizes the compositions of the redox catalysts investigated in this study. CMO core oxide particles were synthesized via a sol-gel method, and the promoted redox catalysts were subsequently obtained through incipient wetness impregnation. Both unpromoted and promoted CMO samples were prepared using Mn(NO₃)₂·4H₂O (Alfa Aesar, 98%) and Cu(NO₃)₂·3H₂O (Sigma-Aldrich). The desired ratio of metal nitrates was dissolved in deionized water with citric acid in a 2.5:1 molar ratio of citric acid (HOC(CH₂CO₂H)₂, Sigma-Aldrich, 99.5%) to metal ions (Cu²⁺ and Mn⁴⁺). Once dissolved, the solution was heated to 40 °C and stirred at 500 rpm for 30 minutes. To promote gel formation from the slurry, a 1.5:1 molar ratio of ethylene glycol (Sigma-Aldrich, 99.8%) to citric acid was added to the mixture. The temperature was then set to 80 °C until gel formation (~1.5 hours), and the resulting gel was dried overnight in a 120 °C oven.

Calcination of the CMO redox core oxide samples was conducted in two steps. In the first step, the sample was heated in a muffle furnace to 450 °C at a ramp rate of 5 °C/min, where it was held at temperature for 3 hours. The resulting powder was then placed into a tube furnace (GSL-15 0X, MTI Corporation) for the second step, where the sample was heated to 1000 °C at 4 °C/min for CMO and held for 8 hours under continuous air flow. The catalyst was then cooled with air.

The MGM core oxide was synthesized by combining Mn(NO₃)₂ (Sigma-Aldrich, 98%) and MgO (Materion Advanced Chemicals, ≥99.5%) precursors in 4 mL of water to create a 15 wt. % manganese catalyst. The mixture was then stirred and dried overnight at 80 °C. The calcination of the MGM paralleled that of CMO, with the MGM sample heating first to 450 °C for 3 hours and then to 900 °C for 8 hours in a muffle furnace before air-cooling to room temperature.

Table 1 also lists the promoters and their respective loadings. To promote the CMO sample with Na₂WO₄ after calcination at 1000 °C, a calculated amount of Na₂WO₄·2H₂O (Sigma-Aldrich, ≥99%) was dissolved in deionized (DI) water to achieve a desired ratio of Na²⁺ ions to catalyst. The resulting solution was then homogenously dripped via pipette onto the CMO sample in a crucible. The crucible was then dried in an oven at 120 °C overnight before calcination at 900 °C to achieve the promoted CMO@Na₂WO₄ sample.

A similar approach was used to promote MGM with Li₂WO₄ (Aldrich Chemistry), Na₂WO₄·2H₂O (Sigma-Aldrich), K₂WO₄ (Acros Organics), Na₂MoO₄ (Aldrich Chemistry), Na₃VO₄ (Aldrich Chemistry), NH₄VO₃ (Sigma-Aldrich), NaNO₃ (Fisher Scientific), and (NH₄)₆Mo₇O₂₄ (Sigma-Aldrich) precursors. Calculated quantities of promoters were dissolved in DI water according to their desired loadings and dried overnight at 80 °C. After subsequent heating to 200 °C to decompose the nitrates, the resulting mixture was calcined, ground, and sieved to 425-850 μm for reaction testing.

Table 1. Promoter type and loading with respect to the oxide type.

Oxide Type	Promoter Type	Promoter Loading (wt. %)
Mn:Cu=4:1 (CMO)	Na ₂ WO ₄ (Na-W)	10 wt. % Na ₂ WO ₄ (1.7 wt. % Na basis)
Mn:Cu=2:1 (CMO)	Na ₂ WO ₄ (Na-W)	
Mn:Cu=1:1 (CMO)	Na ₂ WO ₄ (Na-W)	
Mn:Cu=1:2 (CMO)	Na ₂ WO ₄ (Na-W)	
Mg ₆ MnO ₈ (MGM)	Li ₂ WO ₄	20 wt. % Li ₂ WO ₄
	(Li-W) Na ₂ WO ₄	10 wt. % Na2WO4
	(Na-W)	(6.8 wt. % W basis)[36]
	K ₂ WO ₄	12 wt. % K ₂ WO ₄
	(K-W)	(6.8 wt. % W basis)
	(Li-Na) ₂ WO ₄ (Li-Na-W)	10 wt. % Li ₂ WO ₄ + 10 wt. % Na ₂ WO ₄
	Na ₂ MoO ₄ (Na-Mo)	7.6 wt.% Na ₂ MoO ₄ (1.7 wt. % Na basis)
	NaVO ₃ (Na-V 1-1)	20 wt. % NaVO ₃ (3.8 wt. % Na basis)
	Na ₃ VO ₄ (Na-V 3-1)	20 wt. % Na ₃ VO ₄
	Na ₃ VO ₄ -Na ₂ WO ₄	7 wt.% V ₂ O ₅ +10 wt. % Na ₂ WO ₄
	(75 mol. % Na ₂ WO ₄ , Na-V-W)	(3.8 wt. % Na basis)
	Na ₃ VO ₄ -Na ₂ MoO ₄ -Na ₂ WO ₄ (75 mol. % Na ₂ WO ₄ , Na-V-Mo-W)	3.6 wt.% V ₂ O ₅ +2.6 wt.% M ₀ O ₃ +10 wt. % N _a 2WO ₄
		(3.8 wt. % Na basis)

2.2 Ethane ODH experiment

ODH of ethane was performed in a 1/4" O.D. x 1/8" I.D. U-tube reactor was loaded with 0.5 g of catalyst particles. A 16 mesh white alumina grit was loaded on each side to minimize void

volume and fix the catalyst. In the thermal cracking experiment, the U-tube is filled with the alumina grit to maintain a consistent gas hourly space velocity.

Two-step redox cycle experiments were done to determine the catalysts activities. The redox cycle is separated into two steps: (1) during the reduction step, an Alicat mass flow controllers (MFCs) was used inject 5 mL of 80 vol. % of ethane (balance Ar) is injected into the U-tube. This is followed by 5 minutes of pure Ar gas purge. (2) During the oxidation step, 20 vol. % of O₂ (balance Ar) into the U-tube for 3 minutes to completely regenerate the redox catalyst and remove coke. Following the reduction and oxidation steps, pure Ar gas purged the system for 5 minutes and 4 minutes, respectively. This is followed by four minutes of pure Ar gas purge until the reduction step described in (1). The catalysts have been were tested under six different combinations of temperature (800, 825, 850 °C) and gas hourly space velocity (GHSV=3000 and 4500 hr⁻¹).

The products distribution profile was determined by the gas chromatography (GC). The CO₂/CO and H₂ are analyzed by two thermal conductivity detector (He/TCD for CO₂/CO and Ar/TCD for H₂). The hydrocarbons are analyzed by flame ionization detector. Previous study has verified that there is no significant coking in the system, so the selectivity and the conversion of hydrocarbon is calculated by the carbon mass balance determined by the GC using the same calculation method described in the previous literature, the equations for calculating selectivity and conversion are shown in **Equations 1 and 2**, respectively[36]. The hydrogen to water conversion is calculated based on the hydrogen balance expected from the GC results.

$$S_{C_x H_y} = \frac{x N_{C_x H_y O_z}}{c O + C O_2 + \sum_{1}^{6} n C_n H_m - 2 C_2 H_6} \times 100\%$$
 Equation 1

$$X_{C_2H_6} = (1 - \frac{2N_{C_2H_6}}{c_0 + c_0 + \sum_{1}^{6} n_{C_nH_m}}) \times 100\%$$
 Equation 2

2.3 Catalyst characterization

To determine the bulk crystalline phases, the as-prepared catalysts were analyzed by powder X-ray diffraction (XRD), Rigaku SmartLab X-ray diffractometer with Cu K α (λ = 0.1542 nm) radiation operating at 40 kV and 44 mA. All the catalysts were scanned from 10 to 80° (2 θ) with a step size of 0.1° holding for 3.5 s at each step was used to generate XRD patterns.

To determine the near-surface elemental composition of the as-prepared samples, X-ray photoelectron spectroscopy (XPS) was used. The Kratos Analytical Axis Ultra (monochromated Al K α) was operated at 10mA and 15kV. The results from XPS were analyzed by CasaXPS software, and were calibrated with adventitious peak of carbon 1s at 284.8 eV. The estimated standard deviations for elemental compositions are ~1%.

3. Results and discussion

3.1 Characterization of the crystalline phases of the redox catalysts

CMO and MGM were selected as the core oxides to demonstrate the generalizability of the coreshell redox catalyst design, because CuO and MnO_x based oxides are common options for CL-combustion (CLC) of carbonaceous fuels such as methane, biomass, coal, and syngas.[50–56]. To investigate the effect of different molten salt promoters, we used MGM as the oxide core material[32,36,49]. V and Mo based alkali molten salts were chosen, in addition to tungstate salts, given their similarities.[57] The structural and catalytic effect of different molten salt promoters are elaborated in the following sections.

Figures 2 and **3** summarize the XRD patterns of the promoted CMO and MGM, respectively. As can be seen from **Figure 2**, the characteristic peaks of CuMn₂O₄ are observed from all the CMO based samples. Compared to the unpromoted samples, promoted samples all show the characteristic peaks of Na₂WO₄. These results, along with our previous study with

MGM@Na₂WO₄, further demonstrate that promotion with Na₂WO₄ would remain as a separate phase on different redox oxides without significant ternary phase formation[49]. The observed minor phases formed on the catalyst correlates to the Mn: Cu ratio. As the Mn: Cu ratio decreases, the minor phase shifts from Mn₂O₃ and/or Mn₂O₃ to CuO, a behavior consistent with the phase diagram of the Mn-Cu-O system[58]. The effect of these minority phases will be discussed in the following sections.

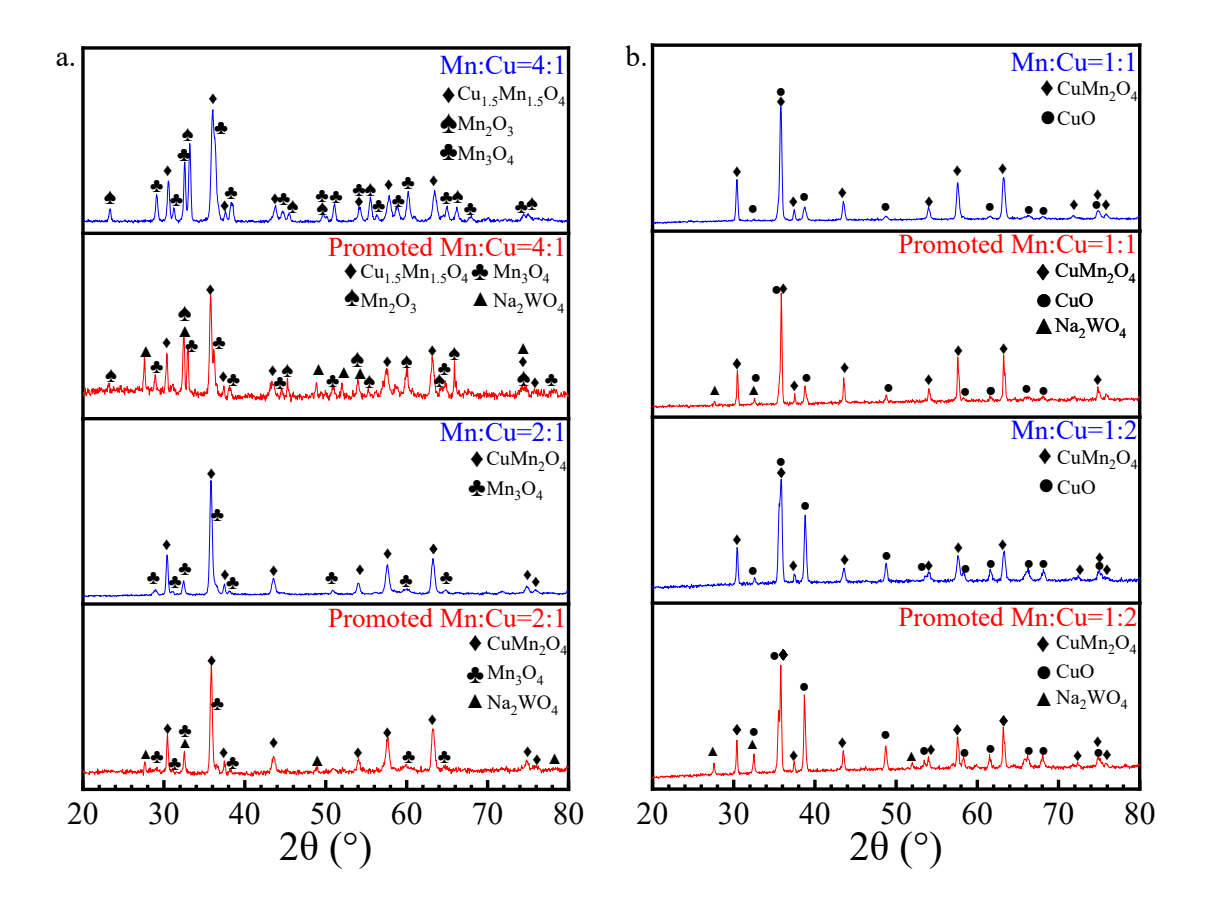


Figure 2. XRD patterns for the promoted and unpromoted CMO samples.

To validate our strategy with other molten salt promoters, W-, Mo-, V-based alkali metal salts and their eutectics on MGM were synthesized and characterized with XRD, as shown in **Figure**3. All of the XRD patterns exhibit the characteristic peaks of MGM. Li-W, Na-W, K-W and Li-Na-W (eutectic) promoted MGM all indicate the presence of the tungstate phase on the MGM with

only minor impurity phases (**Figure 3a**). The XRD pattern of Na-Mo promoted MGM in **Figure 3a** also shows Na₂MoO₄ as a separate phase from MGM. **Figure 3b** summarizes the XRD patterns of MGM promoted with V, V-W, and V-Mo-W mixtures. As expected, 1-1 and 3-1 MGM@Na-V both indicate the presence of Na₃VO₄ phase. Similarly, both MGM@Na-V-W compositions (75 wt. % Na-W and 88 wt. % Na-W) show the formation of Na₂WO₄. A minor NaV₂O₅ phase is observed for MGM@Na-V-W (75 wt. % Na-W), but no vanadate phase was identified for MGM@Na-V-W (88 wt. % Na-W), likely due to the limited amount of V added. The XRD pattern of the ternary mixture promoter, MGM@Na-V-Mo-W, reveals the presence of the Na₂WO₄/Na₂MoO₄ on MGM but not of the vanadate promoter due to its limited loading. The XRD results also confirm that limited reactions take place between the redox oxide and promoter phases, which is an important finding given that the formation of additional phases can disrupt the desired core-shell structure.

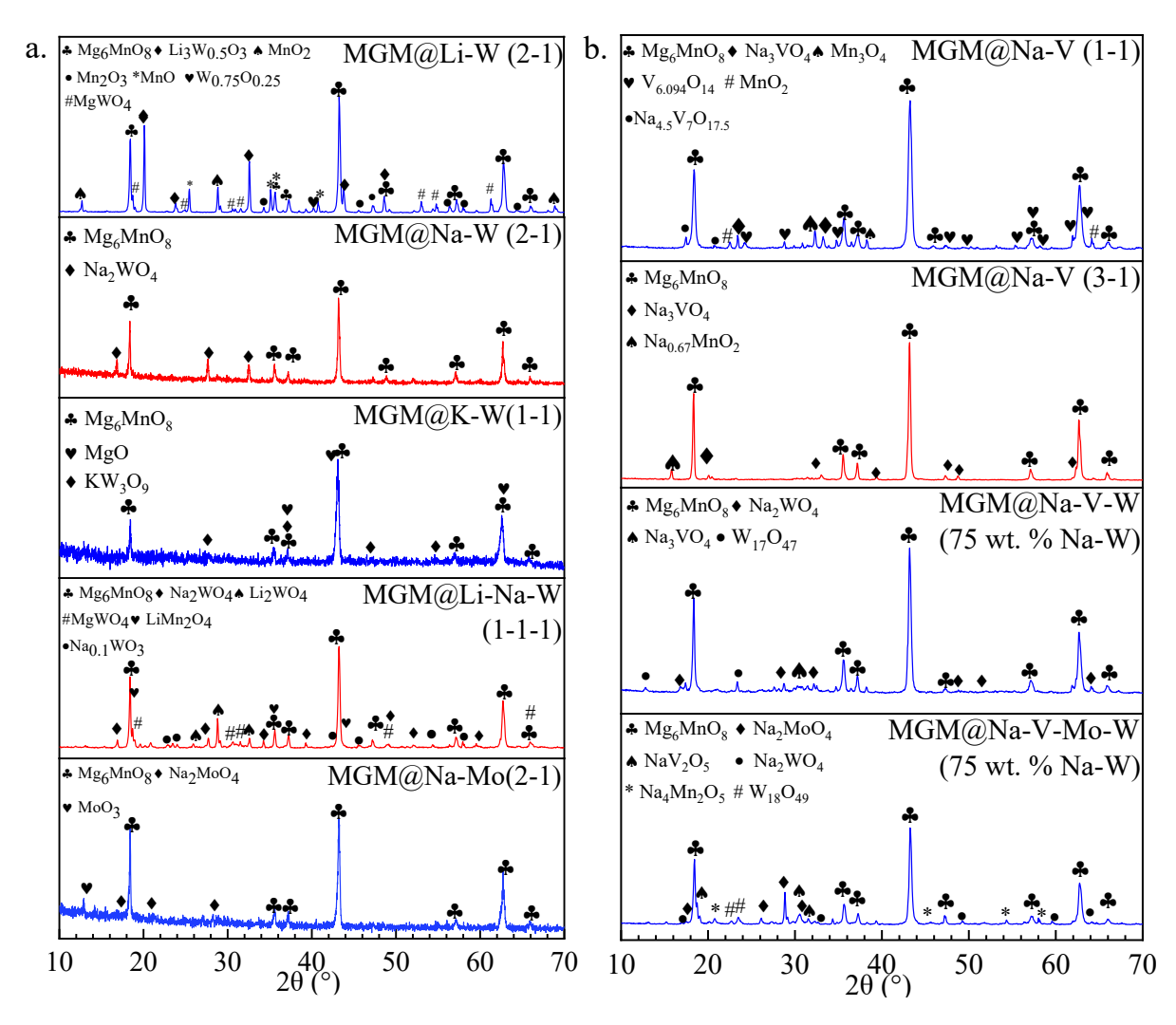


Figure 3. XRD patterns for the promoted MGM samples.

3.2 Characterization of the surface properties

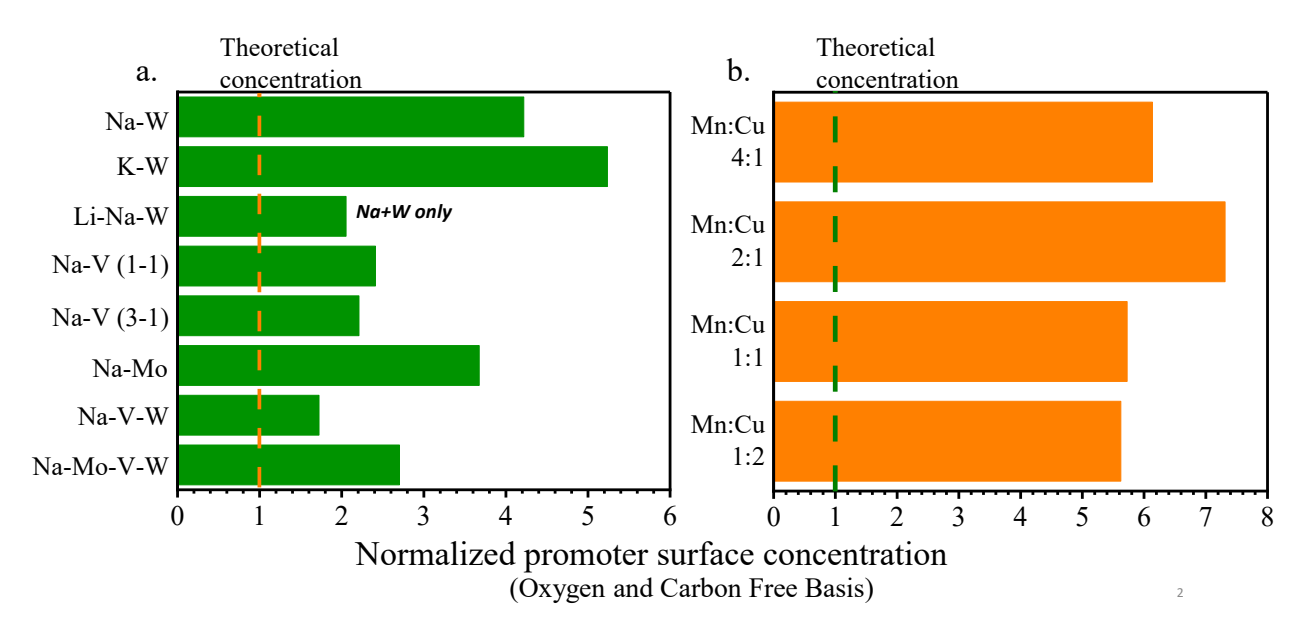


Figure 4. Near-surface atomic composition (oxygen- and carbon-free basis): a) Alkali metals + W/V/Mo in promoted MGM; b) Na+W in Na₂WO₄ promoted CMOs. Theoretical concentration corresponds to the average concentration of the promoter based on the actual loading. The estimated standard deviations for elemental compositions are $\sim 1\%$.

XPS results in **Figures 4a, 4b and Table S2** clearly demonstrate the localization of the promoter phase near the surface of the redox catalysts. As can be seen from **Figure 4**, with the exception of MGM@Li₂WO₄ due to the poor sensitivity of Li in XPS[59], all promoted catalysts show a high surface concentration (150% - 700% surface enrichment) of the promoters compared to the average concentration based on the actual loading shown in **Table 1**. Elemental composition of the X-ray fluorescence of the selected MGM samples are shown in **Table S3**, which also indicates that the bulk composition of the molten salt is lower than that of the surface concentration, which further confirms that the salt are enriched at the surface. This observation indicates that the molten salt promoters are indeed enriched on the surface of the oxide particles and confirms the core-shell structures for all the molten-salt-promoted oxides.

3.3 Catalyst Design – Redox Oxide Selection

The feasibility of *redox oxide* @ *molten salt* strategy was first demonstrated with a series of $Cu_xMn_yO_z$ (CMO) redox oxides promoted with Na_2WO_4 . Figures 5a-5d and Table S4 illustrate the key performance parameters of $Cu_xMn_yO_z$ @ Na_2WO_4 (y:x=4:1,2:1,1:1 and 2:1) at 800-850 °C and GHSV = 4500 hr⁻¹. The reliability of the data was examined and the maximum standard deviations of the selectivity and conversion were $\leq 1.5\%$ (Tables S4). As is apparent from Figure 5a, unlike unpromoted CMO, every Na_2WO_4 -promoted CMO (1.7 wt. % Na basis) exhibited significant increases in C_2H_4 selectivity ($\sim 5\% \rightarrow \sim 90\%$) and yield ($\sim 5\% \rightarrow \sim 56\%$), albeit moderately lower C_2H_6 conversions. Figure 5d also indicates that the H_2 conversions of the promoted CMO series can surpass $\sim 85\%$ at 850 °C, which would sufficiently support autothermal operations for CL-ODH.

The effect of reaction temperature was also investigated. **Figure 5a-5c** implies that as temperature increases from 800 to 850 °C, the maximum C_{2+} selectivity decreases slightly from ~90% to ~80%. However, the temperature increase boosted C_2H_6 conversion by up to 17%, which in turn improved C_{2+} olefin yield (up to 58.9%) as shown in **Figure 5b**. These results further confirm that molten salt promoted redox oxides can enhance C_2H_4 and C_{2+} yields. CH_4 and C_{3+} selectivity also rose slightly, possibly due to the heightened radical formation and thermal cracking activities that take place above 800 °C[7,60–62]. Moreover, as observed in **Figure 5c and 5d**, the temperature increase led to higher H_2 conversions but also higher CO_x selectivity.

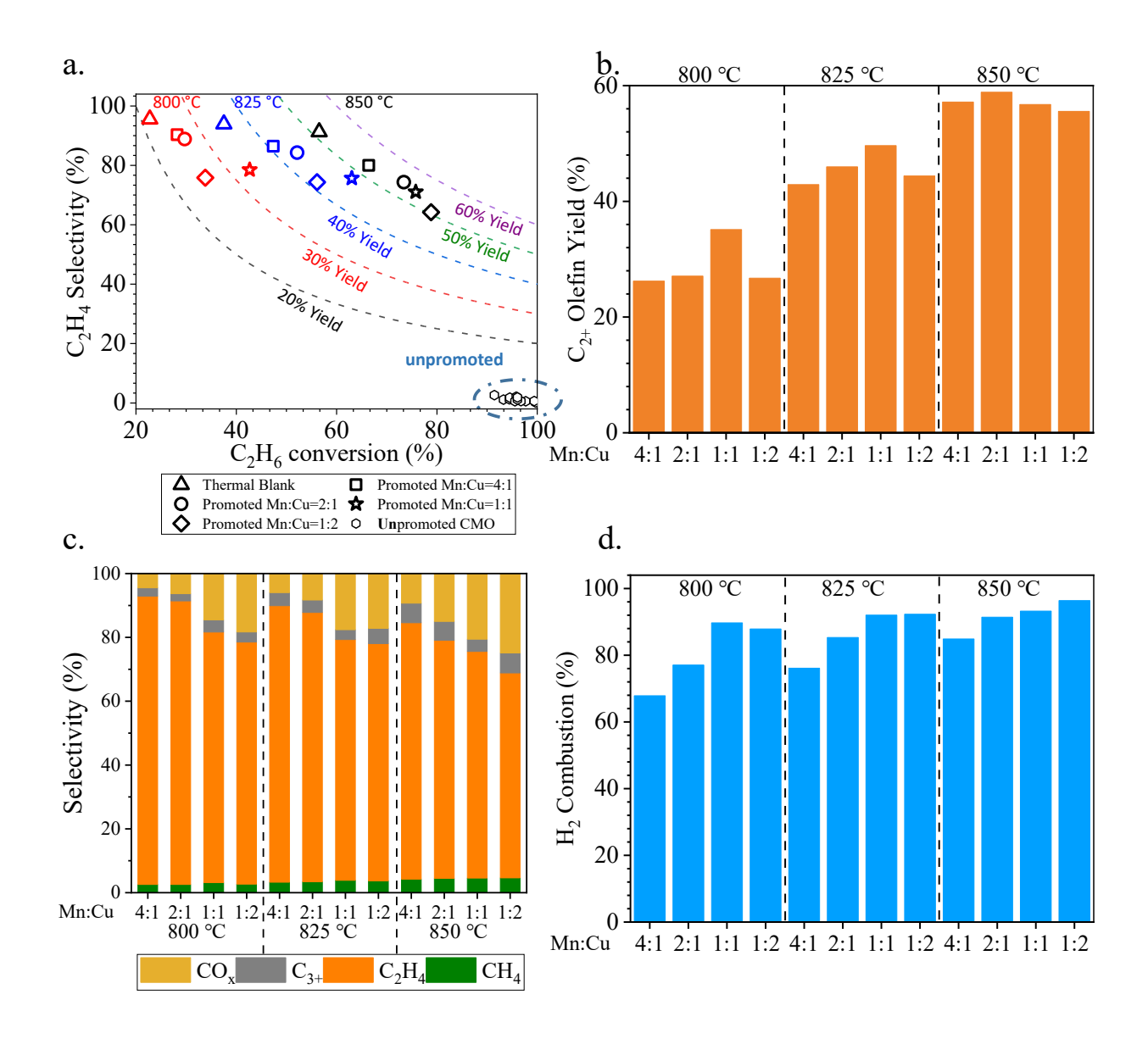


Figure 5. Molten-salt-promoted CMOs reaction testing results at 4500 hr⁻¹ and 800, 825 and 850 °C: a) C₂H₆ conversion and C₂H₄ selectivity profiles; b) C₂₊ olefin yield profiles at 4500 hr⁻¹; c) Product selectivity profiles; d) H₂ conversion of promoted CMOs.

The effect of varying the Cu: Mn ratio was also examined. **Figures 5c and 5d** indicate that as the Cu composition increases in the promoted CMO, C_2H_4 selectivity decreases as H_2 and C_2H_6 conversions improve. The CO_x selectivity shown in **Figure 6a** also corroborates the trend, since the Cu composition increases with the increase of CO_x selectivity. This trend could be explained

by the aforementioned change in the XRD patterns due to Mn:Cu ratio changes in Figure 2. XRD indicated the presence of CuO as Cu content increases. CuO has a strong tendency to decompose and release gaseous oxygen (P_{0_2} = 465 Pa at 850 °C), which would result in deep oxidation (i.e., CO_x selectivity), higher H₂ conversion, and, in turn, higher C₂H₆ conversion[63–65]. We also note that the C₂₊ yield first reaches a maximum as Mn:Cu ratio shifts from 4:1 to 1:1 at 800 °C and 825 °C (2:1 in 850 °C) and then decreases as the Cu:Mn ratio continues to increase, as shown in Figure **5b**. These C₂₊ yield maxima resulted from the competition between C₂H₆ conversion increase and C₂₊ selectivity decrease, as discussed earlier. This volcano-shaped behavior also suggests the possibility of further tailoring the Mn:Cu ratio of the redox catalyst to optimize C₂₊ yield. For the CMO-based redox catalysts, the equilibrium oxygen partial pressure (P_{O2}) of the oxides correlates positively with ethane conversion and negatively with olefin selectivity. Figure 6b also implies that the composition of the redox oxide influences the H_2 combustion and CO_x selectivity. To sum up, these observations argue that a satisfactory redox oxide should (i) maximize selective H₂ combustion to facilitate ethane conversion and autothermal operation and (ii) minimize CO_x selectivity to reduce unwanted byproducts and emissions. In addition, selected oxide compositions should pair synergistically with the operating conditions of the reactor (e.g., temperature and space velocity).

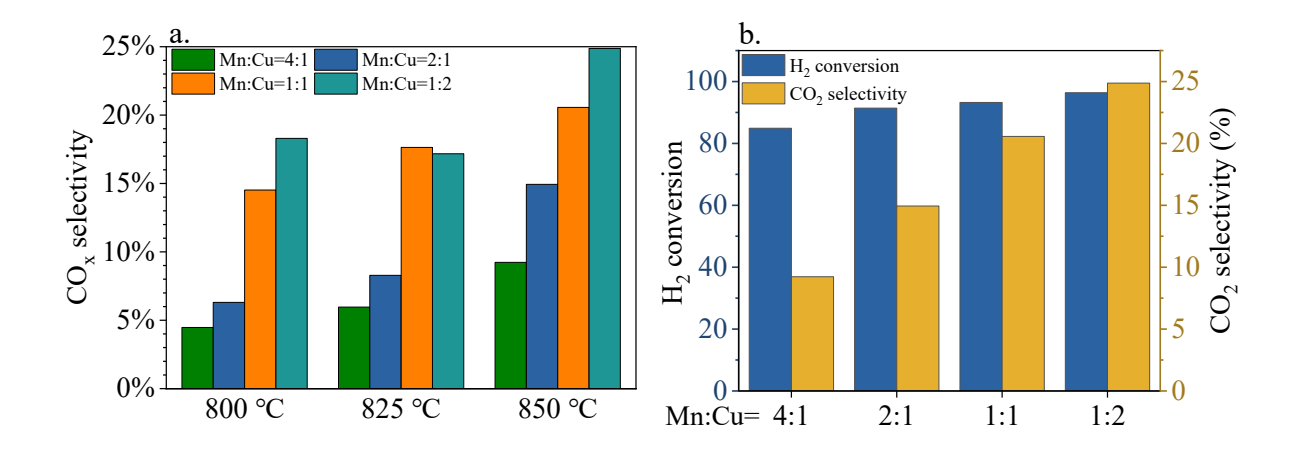


Figure 6. a) The trend of CO_x selectivity on Na₂WO₄ promoted CMO series; b. H₂ conversion and CO₂; b) The relationship between CO₂ selectivity and H₂ conversion at 850 °C, 4500 hr⁻¹.

3.4 Redox Catalyst Design – Selection of Promoters

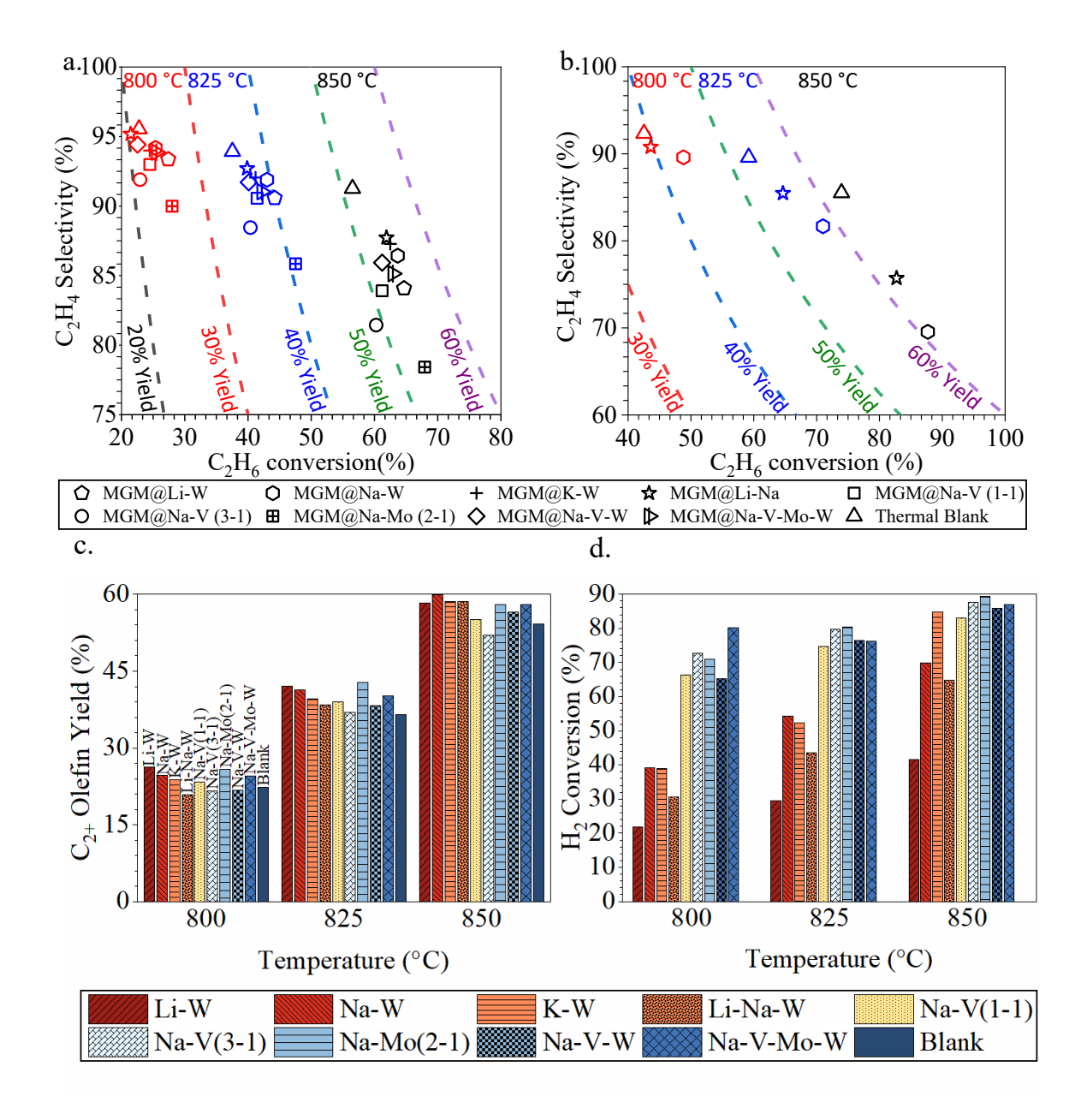


Figure 7. Molten salt promoted MGMs at 800, 825 and 850 °C: a) C₂H₆ conversion and C₂H₄ selectivity profiles at 4500 hr⁻¹ with error bars; b) C₂H₆ conversion and C₂H₄ selectivity profiles at

1500 hr⁻¹; c) C₂₊ olefin yield profiles of promoted MGMs at 4500 hr⁻¹; d) H₂ conversion profiles of promoted MGMs at 4500 hr⁻¹;

Testing different molten salt promoters on MGM further substantiates the *redox oxide* @ *molten salt* strategy. **Figures 7a-7d and Table S5** highlight the key performance metrics for different molten promoters on MGM catalysts at 800-850 °C with gas hourly space velocities of 4500 h⁻¹ and 1500 h⁻¹. The reliability of the data was examined and the maximum standard deviations of the selectivity and conversion were $\leq 1.5\%$ (Table S5). As shown in **Figures 7a** and **7c**, relative to that of the thermal cracking blank, all the catalysts (except Li-Na-W and Li-W promoted MGM at 800 °C and 4500 hr⁻¹) exhibit a slightly lower C_{2+} selectivity. However, the comparative increase in the ethane conversion (up to 11.4% absolute basis) leads to a higher C_{2+} yield in most of the cases. On the other hand, when compared to unpromoted MGM ($\leq 23\%$ C_{2+} selectivity), the promoted catalysts show up to a 72% increase in C_2H_4 selectivity. This significant improvement in performance leads to a maximum single pass C_{2+} yield of 60.4% at 850 °C.

The effects of space velocity and temperature were also investigated. As can be seen in **Figures** 7a and 7b, a lower space velocity leads to lower C_2H_4 selectivity but higher C_2H_4 yield. This result is expected since lower space velocities generally lead to greater extents of conversion and increase sequential oxidation of the C_{2+} products. The effect of temperature is similar to what is observed in the CMO series: as the temperature rises, C_2H_4 selectivity decreases slightly, but the C_2H_4 yield improves significantly due to increased H_2 and C_2H_6 conversions.

The effect of different promoters and their mixtures are further examined at 850 °C. **Figure 7a** and **7c** indicate that the tungstate promoters MGM@Li-W and MGM@Na-W both achieve high C₂H₄ selectivity and yield. Their mixture, MGM@Li-Na-W, attained comparable C₂H₄ and C₂₊ yields as well. This is anticipated, since both MGM@Li-W and MGM@Na-W have a comparable

 C_{2+} selectivities (90.2% and 94.7%) and $C_{2}H_{6}$ conversions (64.7% vs 63.7%). Upon adding Mo to V- and W-containing promoters, a synergistic effect is observed. As can be seen from **Figure 7a** and **7c**, a slight decrease in C_{2+} yield (~3.5% on an abs. scale) when adding V to Na-W promoter to form Na-V-W promoter. However, further addition of Na-Mo to the binary promoter (Na-V-W) system increases C_{2+} yield (~1.4% on an abs. scale). This phenomenon could be attributed to the high C_{2+} yield from the Na-Mo promoter alone, which positively affects the C_{2+} yield in the promoter mixture. It is also noted that the $C_{2}H_{4}$ selectivity is higher for the Na-V-W-Mo promoter when compared to Na-V and Na-Mo promoters.

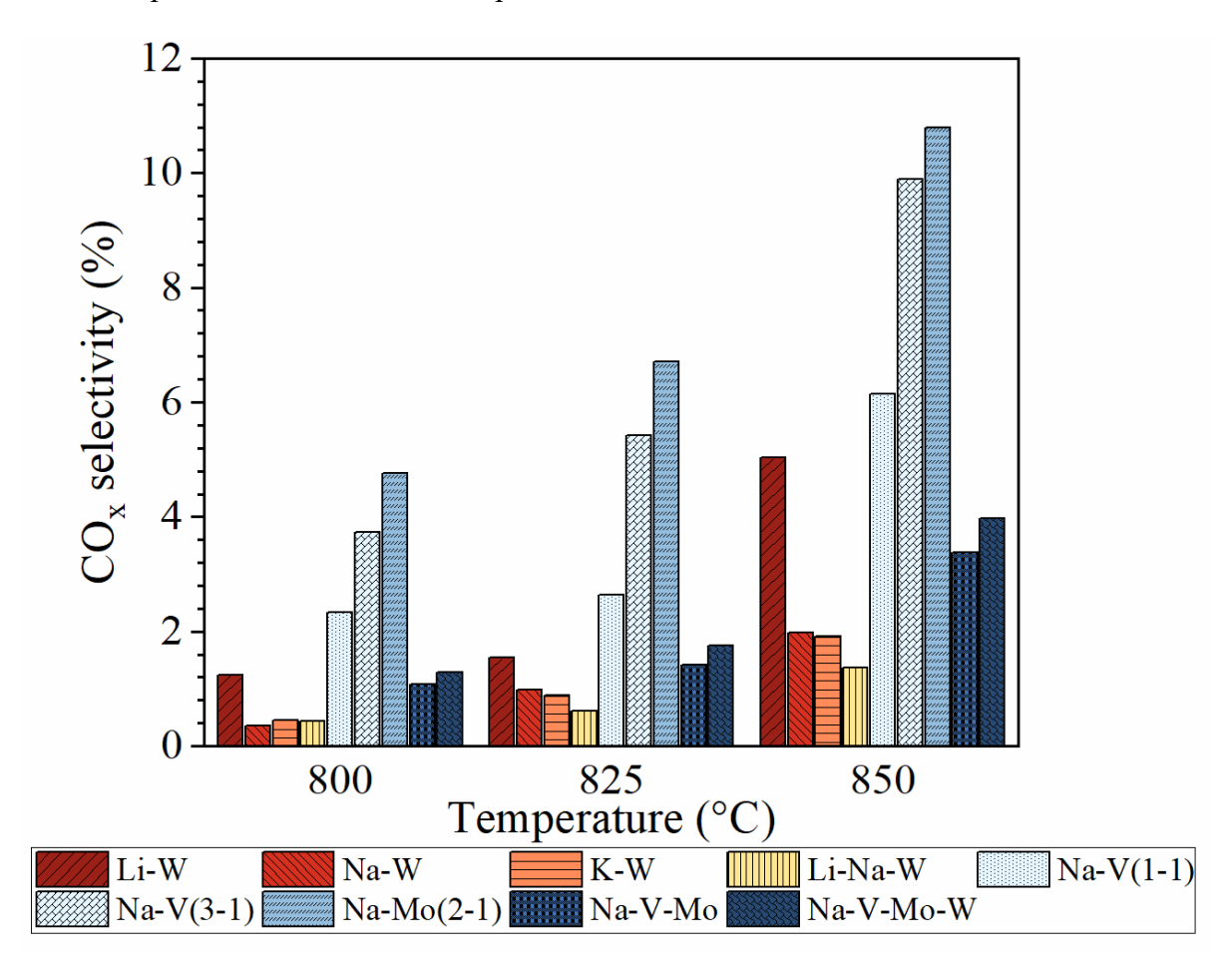


Figure 8. MGM@molten salt CO_x selectivity profile at 800-850 °C, 4500 hr⁻¹

This synergistic effect was also observed in the context of H_2 conversion and CO_x selectivity. As can be inferred from Figure 7d, among the tungstate promoters, K₂WO₄ (K-W) exhibits the highest H₂ conversion at 850 °C, followed by Na-W and Li-W. For the binary molten mixture system, adding Na-W to Li-W (i.e. Li-Na-W) results in a ~24% increase in H₂ conversion. Interestingly, the addition of Na-W to Li-W also decreases the CO_x selectivity, as shown in **Figure** 8, an effect also observed in Mo-, V-, and W-containing samples. A ~16% increase (absolute basis) of H₂ conversion is observed after supplementing the Na-W promoter with V to form Na-V-W promoter (~70% to 86%). This improvement could stem from the addition of Na-V (3-1), a promoter that previously demonstrated a high H₂ conversion of ~88%. Further addition of Na-Mo to the binary promoter (Na-V-W) system also increases H₂ conversion, as the Na-Mo promoter alone exhibits up to 89.3% H₂ conversion. In terms of CO_x selectivity, Figure 8 shows that the CO_x selectivity of the MGM@Na-V-Mo eutectic is lower than those of both MGM@Na-V and MGM@Na-Mo. Adding Na-W to MGM@Na-V-Mo slightly increases the CO_x selectivity, but the CO_x selectivity remains significantly lower than those of Na-V and Na-Mo alone. From both of the tungstate cases and the V/W/Mo mixture cases, it can be concluded combinations of different molten salts can result in both a lower CO_x selectivity and a higher H₂ conversion. These attributes can benefit the overall CL-ODH scheme.

The CO_x selectivity and the H₂ conversion of MGM@Li-W differs significantly from other W-promoted MGM. The CO_x selectivity of MGM@Li-W was 5%, which is ~150% (relative basis) higher than those of other W-promoted MGM (~2%). The H₂ conversion of MGM@Li-W was 41.6%, which is 30~50% (absolute basis) lower than the average H₂ conversion of W-promoted catalysts. **Figure 9** further indicates that the amounts of lattice oxygen donated from Li₂WO₄-containing samples (i.e. Li-W, Li-Na-W) are up to 69% lower than non-Li containing catalysts,

using **Equation S1 and S2**. These results reveal that Li₂WO₄ does not effectively promote selective H₂ conversion or ethylene production.

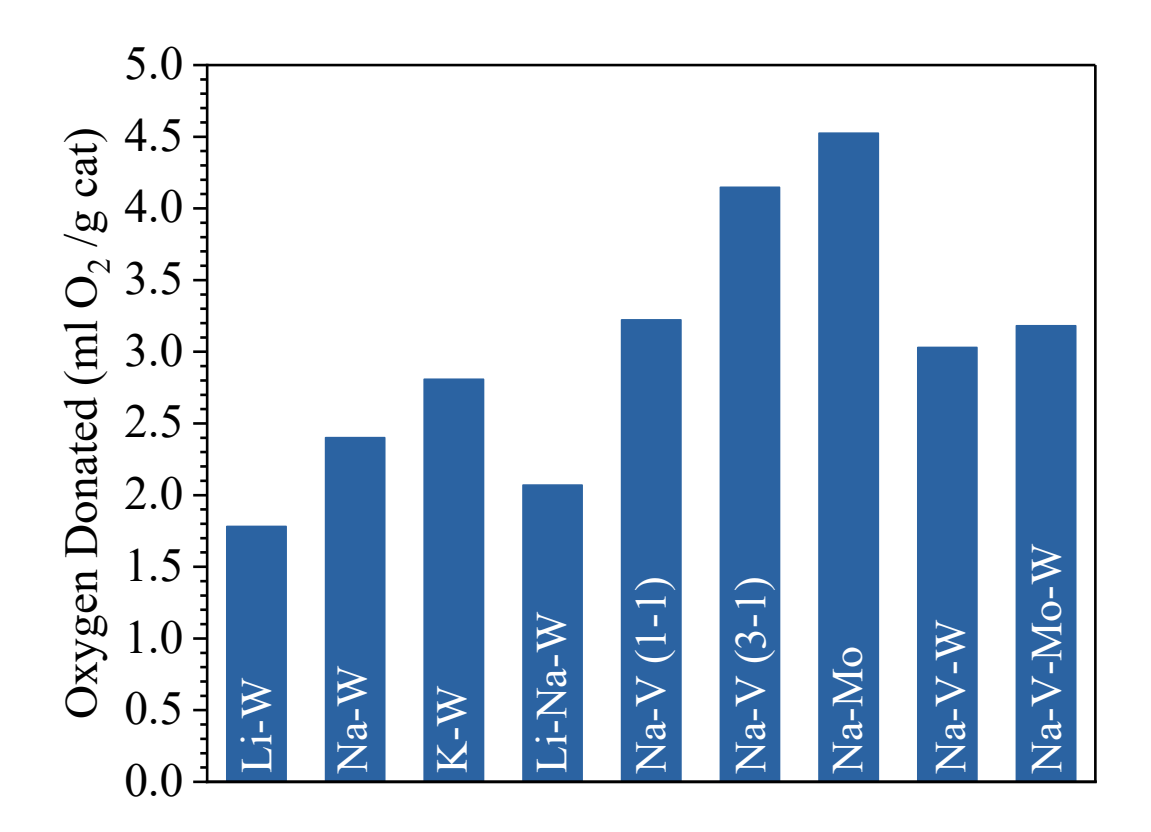


Figure 9. Lattice oxygen donation (mL O₂/g catalyst) of the promoted MGM samples at 4500 hr⁻¹, 850 °C.

3.5 Potential Redox Catalyst Optimizations

The data presented above also demonstrate that the C₂₊ selectivity is inversely proportional to the CO₂ selectivity. **Figure 10a** summarizes the selectivity data of both promoted and unpromoted MGMs and CMOs at >80% H₂ conversion. From this figure, we see that increase in H₂ conversion corresponds to decreasing C₂₊ selectivity and increasing CO_x selectivity. Both **Figures 10a** and **S4a** imply that competition exists between H₂ combustion and ethylene combustion. In other words, reducing the concentration of H₂ promotes non-selective combustion of the olefin products by the redox catalyst. Additionally, shown in **Figure S1a**, when H₂ conversion falls below 80%,

both CO₂ and C₂₊ selectivity stay relatively stable at <10% and >90%, respectively. **Figure S1b** also shows that the CH₄ selectivity stays below 4.6% regardless of the H₂ conversion. Further comparisons between 4500 hr⁻¹ and 1500 hr⁻¹ using tungstate-containing promoted MGM are provided in Figure 10b. Although the R² values of the fitted curves in Figure 10b were less than ideal, the slopes of the curves are significantly different statistically (at 4500 hr⁻¹ slope = -0.09, at $1500 \text{ hr}^{-1} \text{ slope} = -0.23$, see **Table S5** for the statistical test result). This discrepancy suggests that as conversion increases, a higher space velocity should result in higher C2+ selectivity and, consequently, a higher C₂₊ yield. Figures 10c summarizes the performance of tungstate-containing promoted MGMs and CMOs, respectively. Again, a significant difference between the slopes is observed (MGM slope = -0.09, CMO slope = -0.31; see **Table S6** for the statistical test result). This implies that tungstate-promoted MGMs result in higher C₂₊ selectivities than tungstatepromoted CMOs, due to higher CO_x selectivities of the former. This corroborates well with the discussions in the previous sections. Tables S6 and S7 provide the key statistics for the linear fit of the C_{2+} selectivity and C_{2+} yield for each catalyst. **Table S6 and S7** also indicate that, excluding MGM@Na-V (3-1), all of the MGM catalysts have less negative slopes than that of CMO, which confirms that the MGM redox catalysts perform better than that of CMO in terms of the C₂₊ selectivity and C₂₊ yield. Both tables indicate that MGM@Li-Na-W have the potential to reach optimal C_{2+} yield when the conversion increases. Figure 10d shows the general trend for C_{2+} yield, with the C₂₊ yield performance data of MGMs fitted together using both a linear and sigmoidal model and the performance data of CMOs fitted with a sigmoidal model. Detailed parameters and key statistics are provided in **Table S8**. All models fit well ($R^2 > 0.9$). We predict that further optimization would result in the expected yield shown in the shaded region of Figure 10d. This prediction indicated that it is possible to further optimize the C_{2+} yield to 78.2 - 86.7%. These

analyses indicate that further increase in single-pass olefin yield would be possible by simply optimizing the operating conditions with the redox catalysts reported in this study. Given the flexibility and generalizability of the core-shell redox catalyst system, further tailoring the redox oxide @ molten salt compositions to minimize CO_x without increasing CH₄ selectivity is also likely.

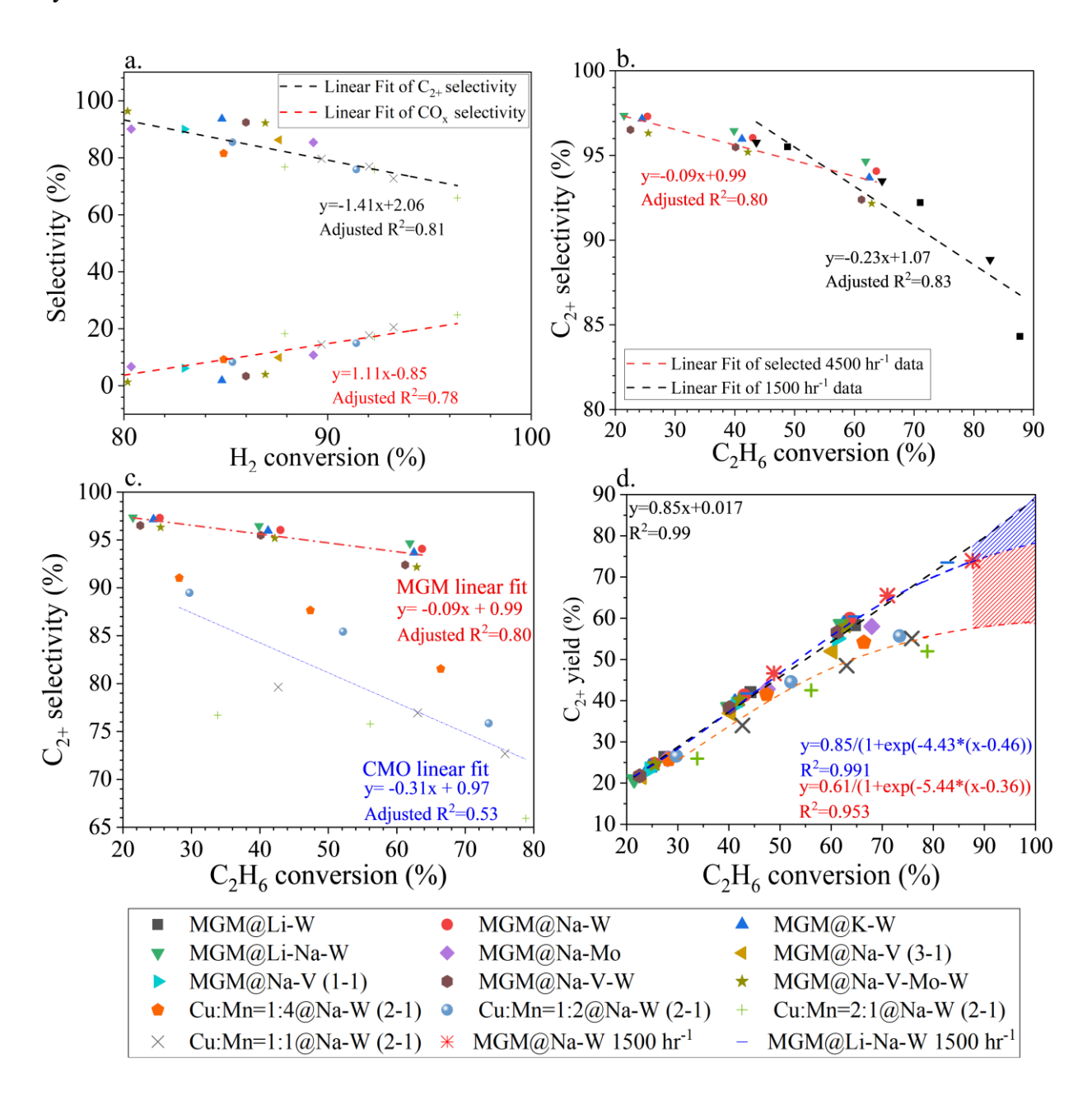


Figure 10. a) C₂₊ selectivity and CO₂ selectivity vs H₂ conversion at GHSV=4500 hr⁻¹; b) C₂₊ selectivity of tungstate-promoted MGMs at GHSV=4500 hr⁻¹, 1500 hr⁻¹ and 800, 825, and 850 °C. c) C₂₊ selectivity of tungstate-promoted MGMs and CMOs at GHSV=4500 hr⁻¹; d) Linear fit (black) and sigmoidal fit (blue) of all promoted MGMs, and sigmoidal fit (red) of all CMO performance data at different temperature and space velocities (1500 and 4500 hr⁻¹). The blue region highlights the anticipated yield with the better performing redox catalysts (i.e. 88% conversion, 73.9% yield to 100% conversion, 86.7% yield). The red region highlights the anticipated yield with the less effective redox catalysts (i.e. 88% conversion, 57.6% yield to 100% conversion, 78.2% yield)

4. Conclusion

The present study demonstrates a redox oxide @ molten salt core-shell architecture as a generalized redox catalyst design strategy for chemical looping – oxidative dehydrogenation of ethane. XPS data collected on all 17 redox catalyst samples with different oxide and molten salt combinations confirmed that the molten salt promoters aggregate at the outer surface of the oxide, forming a core-shell structure. XRD results further confirmed that the promoter salts and core oxides are fully compatible by forming separate phases without significant chemical interactions. Catalyst performance tests with CMO@Na2WO4 indicated that a higher Cu content leads to higher C2H6 conversion but also increases CO2 selectivity. This highlights the importance to optimize the redox properties of the core oxides to maximize the C2+ yield. For the MGM-based redox catalysts, we reported a synergistic effect for molten salt mixtures: combination of different molten salts can further enhance the C2+ yield, increase the H2 conversion, and decrease the CO2 selectivity. Up to 74% single pass yield of C2+ olefins was demonstrated, along with low COx selectivity. Statistical fitting of the performance data for the various redox catalyst compositions indicate that 78.2 –

86.7% single pass olefin yield can potentially be achieved by optimizing the operating conditions (e.g. higher operating temperature coupled with higher space velocity). The generalizability of the core-shell redox catalyst design strategy also offers exciting opportunities to further optimize the composition and performance of the redox catalysts in the context of CL-ODH.

Author Contributions

The manuscript was written through contributions of all authors. All authors have given approval to the final version of the manuscript. ‡These authors contributed equally.

Acknowledgement

This work was supported by the US National Science Foundation (Award No. CBET- 2116724), the National Energy Technology Lab (DE-FE0031918), and the Kenan Institute for Engineering, Technology and Science at the NC State University. The characterization was performed in part at the Analytical Instrumentation Facility (AIF) at North Carolina State University and the Duke University Shared Materials Instrumentation Facility (SMIF), which are supported by the State of North Carolina and the National Science Foundation (award number ECCS-2025064). AIF and SMIF are members of the North Carolina Research Triangle Nanotechnology Network (RTNN), a site in the National Nanotechnology Coordinated Infrastructure (NNCI).

References

[1] R. Perry, Ethane Storage and Distribution Hub in the United States, (2018). https://www.energy.gov/sites/prod/files/2018/12/f58/Nov%202018%20DOE%20Ethane%2 0Hub%20Report.pdf.

- [2] J.J. Siirola, The impact of shale gas in the chemical industry, AIChE J. 60 (2014) 810–819. https://doi.org/10.1002/aic.14368.
- [3] J. Ciferno, Developing Technologies for Upcycling Associated Gas into Higher-Value Products., U.S. Department of Energy. (2020) https://www.netl.doe.gov/sites/default/files/2020-12/Upcycling-Associated-Gas-into-Higher-Value-Products-12-2020.pdf.
- [4] Crude Oil To Natural Gas Ratio Explodes to 52:1, EconMatters. (2012). https://www.nasdaq.com/articles/crude-oil-natural-gas-ratio-explodes-521-2012-04-15.
- [5] US natural gas total consumption., (2021). https://www.eia.gov/dnav/ng/hist/n9140us2a.htm.
- [6] T. Ren, M. Patel, K. Blok, Olefins from conventional and heavy feedstocks: Energy use in steam cracking and alternative processes, Energy. 31 (2006) 425–451. https://doi.org/10.1016/j.energy.2005.04.001.
- [7] C.A. Gärtner, A.C. van Veen, J.A. Lercher, Oxidative Dehydrogenation of Ethane: Common Principles and Mechanistic Aspects, ChemCatChem. 5 (2013) 3196–3217. https://doi.org/10.1002/cctc.201200966.
- [8] V.P. Haribal, L.M. Neal, F. Li, Oxidative dehydrogenation of ethane under a cyclic redox scheme Process simulations and analysis, Energy. 119 (2017) 1024–1035. https://doi.org/10.1016/j.energy.2016.11.039.
- [9] D. Melzer, G. Mestl, K. Wanninger, Y. Zhu, N.D. Browning, M. Sanchez-Sanchez, J.A. Lercher, Design and synthesis of highly active MoVTeNb-oxides for ethane oxidative dehydrogenation, Nat Commun. 10 (2019) 4012. https://doi.org/10.1038/s41467-019-11940-0.
- [10] S. Najari, S. Saeidi, P. Concepcion, D.D. Dionysiou, S.K. Bhargava, A.F. Lee, K. Wilson, Oxidative dehydrogenation of ethane: catalytic and mechanistic aspects and future trends, Chem. Soc. Rev. 50 (2021) 4564–4605. https://doi.org/10.1039/D0CS01518K.
- [11] F. Cavani, N. Ballarini, A. Cericola, Oxidative dehydrogenation of ethane and propane: How far from commercial implementation?, Catalysis Today. 127 (2007) 113–131. https://doi.org/10.1016/j.cattod.2007.05.009.
- [12] K.-I. Nakamura, T. Miyake, T. Konishi, T. Suzuki, Oxidative dehydrogenation of ethane to ethylene over NiO loaded on high surface area MgO, Journal of Molecular Catalysis A: Chemical. 260 (2006) 144–151. https://doi.org/10.1016/j.molcata.2006.06.058.
- [13] Z. Skoufa, E. Heracleous, A.A. Lemonidou, Investigation of engineering aspects in ethane ODH over highly selective Ni0.85Nb0.15Ox catalyst, Chemical Engineering Science. 84 (2012) 48–56. https://doi.org/10.1016/j.ces.2012.08.007.
- [14] X. Zhang, J. Liu, Y. Jing, Y. Xie, Support effects on the catalytic behavior of NiO/Al2O3 for oxidative dehydrogenation of ethane to ethylene, Applied Catalysis A: General. 240 (2003) 143–150. https://doi.org/10.1016/S0926-860X(02)00426-X.
- [15] H. Zhu, H. Dong, P. Laveille, Y. Saih, V. Caps, J.-M. Basset, Metal oxides modified NiO catalysts for oxidative dehydrogenation of ethane to ethylene, Catalysis Today. 228 (2014) 58–64. https://doi.org/10.1016/j.cattod.2013.11.061.
- [16] Z.-S. Chao, E. Ruckenstein, A Comparison of Catalytic Oxidative Dehydrogenation of Ethane Over Mixed V-Mg Oxides and Over Those Prepared via a Mesoporous V-Mg-O Pathway, (n.d.) 9.
- [17] Z.-S. Chao, E. Ruckenstein, Noncatalytic and catalytic conversion of ethane over V□Mg oxide catalysts prepared via solid reaction or mesoporous precursors, Journal of Catalysis. 222 (2004) 17–31. https://doi.org/10.1016/j.jcat.2003.11.004.

- [18] B. Solsona, A. Dejoz, T. Garcia, P. Concepcion, J. Nieto, M. Vazquez, M. Navarro, Molybdenum–vanadium supported on mesoporous alumina catalysts for the oxidative dehydrogenation of ethane, Catalysis Today. 117 (2006) 228–233. https://doi.org/10.1016/j.cattod.2006.05.025.
- [19] H.X. Dai, C.F. Ng, C.T. Au, Perovskite-Type Halo-oxide La1-xSrxFeO3-δXσ (X=F, Cl) Catalysts Selective for the Oxidation of Ethane to Ethene, Journal of Catalysis. 189 (2000) 52–62. https://doi.org/10.1006/jcat.1999.2677.
- [20] S.A.R. Mulla, O.V. Buyevskaya, M. Baerns, Autothermal Oxidative Dehydrogenation of Ethane to Ethylene Using SrxLa1.0Nd1.0Oy Catalysts as Ignitors, Journal of Catalysis. 197 (2001) 43–48. https://doi.org/10.1006/jcat.2000.3059.
- [21] D.A. Henning, L.D. Schmidt, Oxidative dehydrogenation of ethane at short contact times: species and temperature proÿles within and after the catalyst, Chemical Engineering Science. (2002) 11.
- [22] M. Huff, L.D. Schmidt, Ethylene formation by oxidative dehydrogenation of ethane over monoliths at very short contact times, J. Phys. Chem. 97 (1993) 11815–11822. https://doi.org/10.1021/j100147a040.
- [23] C. Yokoyama, S.S. Bharadwaj, L.D. Schmidt, Platinum-tin and platinum-copper catalysts for autothermal oxidative dehydrogenation of ethane to ethylene, Catal Lett. 38 (1996) 181–188. https://doi.org/10.1007/BF00806566.
- [24] F. Donsì, K.A. Williams, L.D. Schmidt, A Multistep Surface Mechanism for Ethane Oxidative Dehydrogenation on Pt- and Pt/Sn-Coated Monoliths, Ind. Eng. Chem. Res. 44 (2005) 3453–3470. https://doi.org/10.1021/ie0493356.
- [25] P. Botella, Selective oxidative dehydrogenation of ethane on MoVTeNbO mixed metal oxide catalysts, Journal of Catalysis. 225 (2004) 428–438. https://doi.org/10.1016/j.jcat.2004.04.024.
- [26] Q. Xie, L. Chen, W. Weng, H. Wan, Preparation of MoVTe(Sb)Nb mixed oxide catalysts using a slurry method for selective oxidative dehydrogenation of ethane, Journal of Molecular Catalysis A: Chemical. (2005) S1381116905004760. https://doi.org/10.1016/j.molcata.2005.07.004.
- [27] S. Gaab, M. Machli, J. Find, R.K. Grasselli, J.A. Lercher, Oxidative dehydrogenation of ethane over novel Li/Dy/Mg mixed oxides: structure–activity study, Topics in Catalysis. 23 (2008) 151–158.
- [28] C.A. Gärtner, A.C. van Veen, J.A. Lercher, Oxidative Dehydrogenation of Ethane on Dynamically Rearranging Supported Chloride Catalysts, J. Am. Chem. Soc. 136 (2014) 12691–12701. https://doi.org/10.1021/ja505411s.
- [29] B. Frank, M. Morassutto, R. Schomäcker, R. Schlögl, D.S. Su, Oxidative Dehydrogenation of Ethane over Multiwalled Carbon Nanotubes, ChemCatChem. 2 (2010) 644–648. https://doi.org/10.1002/cctc.201000035.
- [30] L. Shi, B. Yan, D. Shao, F. Jiang, D. Wang, A.-H. Lu, Selective oxidative dehydrogenation of ethane to ethylene over a hydroxylated boron nitride catalyst, Chinese Journal of Catalysis. 38 (2017) 389–395. https://doi.org/10.1016/S1872-2067(17)62786-4.
- [31] W.F. Castle, Air separation and liquefaction: recent developments and prospects for the beginning of the new millennium, International Journal of Refrigeration. 25 (2002) 158–172. https://doi.org/10.1016/S0140-7007(01)00003-2.

- [32] L.M. Neal, S. Yusuf, J.A. Sofranko, F. Li, Oxidative Dehydrogenation of Ethane: A Chemical Looping Approach, Energy Technol. 4 (2016) 1200–1208. https://doi.org/10.1002/ente.201600074.
- [33] T. Wang, Y. Gao, Y. Liu, M. Song, J. Liu, Q. Guo, Core-shell Na2WO4/CuMn2O4 oxygen carrier with high oxygen capacity for chemical looping oxidative dehydrogenation of ethane, Fuel. 303 (2021) 121286. https://doi.org/10.1016/j.fuel.2021.121286.
- [34] P. NOVOTNÝ, Molybdenum Oxide Supported on Hematite and Alumina as Redox Catalysts for Chemical Looping Oxidative Dehydrogenation of Ethane, North Carolina University, 2019.
- [35] P. Novotný, S. Yusuf, F. Li, H.H. Lamb, MoO ₃ /Al ₂ O ₃ catalysts for chemical-looping oxidative dehydrogenation of ethane, J. Chem. Phys. 152 (2020) 044713. https://doi.org/10.1063/1.5135920.
- [36] S. Yusuf, L. Neal, Z. Bao, Z. Wu, F. Li, Effects of Sodium and Tungsten Promoters on Mg ₆ MnO ₈ -Based Core–Shell Redox Catalysts for Chemical Looping—Oxidative Dehydrogenation of Ethane, ACS Catal. 9 (2019) 3174–3186. https://doi.org/10.1021/acscatal.9b00164.
- [37] L.M. Neal, V.P. Haribal, F. Li, Intensified Ethylene Production via Chemical Looping through an Exergetically Efficient Redox Scheme, IScience. 19 (2019) 894–904. https://doi.org/10.1016/j.isci.2019.08.039.
- [38] Y. Gao, L.M. Neal, F. Li, Li-Promoted La _x Sr _{2-x} FeO _{4-δ} Core–Shell Redox Catalysts for Oxidative Dehydrogenation of Ethane under a Cyclic Redox Scheme, ACS Catal. 6 (2016) 7293–7302. https://doi.org/10.1021/acscatal.6b01399.
- [39] G. Luongo, F. Donat, A.H. Bork, E. Willinger, A. Landuyt, C.R. Müller, Highly Selective Oxidative Dehydrogenation of Ethane to Ethylene via Chemical Looping with Oxygen Uncoupling through Structural Engineering of the Oxygen Carrier, Advanced Energy Materials. (2022) 2200405. https://doi.org/10.1002/aenm.202200405.
- [40] R.B. Dudek, F. Li, Selective hydrogen combustion as an effective approach for intensified chemical production via the chemical looping strategy, Fuel Processing Technology. 218 (2021) 106827. https://doi.org/10.1016/j.fuproc.2021.106827.
- [41] W. Ding, K. Zhao, S. Jiang, Z. Zhao, Y. Cao, F. He, Alkali-metal enhanced LaMnO3 perovskite oxides for chemical looping oxidative dehydrogenation of ethane, Applied Catalysis A: General. 609 (2021) 117910. https://doi.org/10.1016/j.apcata.2020.117910.
- [42] X. Tian, C. Zheng, F. Li, H. Zhao, Co and Mo Co-doped Fe ₂ O ₃ for Selective Ethylene Production via Chemical Looping Oxidative Dehydrogenation, ACS Sustainable Chem. Eng. 9 (2021) 8002–8011. https://doi.org/10.1021/acssuschemeng.1c02726.
- [43] X. Tian, C. Zheng, H. Zhao, Ce-modified SrFeO3- for ethane oxidative dehydrogenation coupled with CO2 splitting via a chemical looping scheme, Applied Catalysis B: Environmental. 303 (2022) 120894. https://doi.org/10.1016/j.apcatb.2021.120894.
- [44] Y. Tian, P.R. Westmoreland, F. Li, CaMn0.9Ti0.1O3 based redox catalysts for chemical looping Oxidative dehydrogenation of ethane: Effects of Na2MoO4 promoter and degree of reduction on the reaction kinetics, Catalysis Today. (2022) S0920586122001444. https://doi.org/10.1016/j.cattod.2022.04.026.
- [45] W. Sun, G. Zhao, Y. Gao, J. Si, Y. Liu, Y. Lu, An oxygen carrier catalyst toward efficient chemical looping-oxidative coupling of methane, Applied Catalysis B: Environmental. 304 (2022) 120948. https://doi.org/10.1016/j.apcatb.2021.120948.

- [46] M. Li, Y. Gao, K. Zhao, H. Li, F. He, P. Lv, Z. Huang, Mg-doped La1.6Sr0.4FeCoO6 for anaerobic oxidative dehydrogenation of ethane using surface-absorbed oxygen with tuned electronic structure, Fuel Processing Technology. 216 (2021) 106771. https://doi.org/10.1016/j.fuproc.2021.106771.
- [47] A.H. Elbadawi, M.S. Ba-Shammakh, S. Al-Ghamdi, S.A. Razzak, M.M. Hossain, Reduction kinetics and catalytic activity of VO x /γ-Al 2 O 3 -ZrO 2 for gas phase oxygen free ODH of ethane, Chemical Engineering Journal. 284 (2016) 448–457. https://doi.org/10.1016/j.cej.2015.08.048.
- [48] S. Al-Ghamdi, M. Volpe, M.M. Hossain, H. de Lasa, VOx/c-Al2O3 catalyst for oxidative dehydrogenation of ethane to ethylene: Desorption kinetics and catalytic activity, Applied Catalysis A: General. 450 (2013) 120–130. https://doi.org/10.1016/j.apcata.2012.10.007.
- [49] S. Yusuf, L.M. Neal, F. Li, Effect of Promoters on Manganese-Containing Mixed Metal Oxides for Oxidative Dehydrogenation of Ethane via a Cyclic Redox Scheme, ACS Catal. 7 (2017) 5163–5173. https://doi.org/10.1021/acscatal.7b02004.
- [50] H. Fang, L. Haibin, Z. Zengli, Advancements in Development of Chemical-Looping Combustion: A Review, International Journal of Chemical Engineering. 2009 (2009) 1–16. https://doi.org/10.1155/2009/710515.
- [51] F. García-Labiano, L.F. de Diego, J. Adánez, A. Abad, P. Gayán, Reduction and Oxidation Kinetics of a Copper-Based Oxygen Carrier Prepared by Impregnation for Chemical-Looping Combustion, Ind. Eng. Chem. Res. 43 (2004) 8168–8177. https://doi.org/10.1021/ie0493311.
- [52] J. Adánez, P. Gayán, I. Adánez-Rubio, A. Cuadrat, T. Mendiara, A. Abad, F. García-Labiano, L.F. de Diego, Use of Chemical-Looping processes for coal combustion with CO2 capture, Energy Procedia. 37 (2013) 540–549. https://doi.org/10.1016/j.egypro.2013.05.140.
- [53] M.M. Hossain, H.I. de Lasa, Chemical-looping combustion (CLC) for inherent CO2 separations—a review, Chemical Engineering Science. 63 (2008) 4433–4451. https://doi.org/10.1016/j.ces.2008.05.028.
- [54] P. Mungse, G. Saravanan, T. Uchiyama, M. Nishibori, Y. Teraoka, S. Rayalu, N. Labhsetwar, Copper–manganese mixed oxides: CO ₂ -selectivity, stable, and cyclic performance for chemical looping combustion of methane, Phys. Chem. Chem. Phys. 16 (2014) 19634–19642. https://doi.org/10.1039/C4CP01747A.
- [55] A.-M. Azad, A. Hedayati, M. Rydén, H. Leion, T. Mattisson, Examining the Cu-Mn-O Spinel System as an Oxygen Carrier in Chemical Looping Combustion, Energy Technology. 1 (2013) 59–69. https://doi.org/10.1002/ente.200009.
- [56] R. Siriwardane, H. Tian, G. Richards, T. Simonyi, J. Poston, Chemical-Looping Combustion of Coal with Metal Oxide Oxygen Carriers, Energy Fuels. 23 (2009) 3885–3892. https://doi.org/10.1021/ef9001605.
- [57] J.R. Rumble, T.J. Bruno, M.J. Doa, CRC Handbook of Chemistry and Physics, 102nd ed., CRC Press, Taylor & Francis Group, 2021.
- [58] F.C.M. Driessens, G.D. Rieck, Phase Equilibria in the System Cu?Mn?O, Z. Anorg. Allg. Chem. 351 (1967) 48–62. https://doi.org/10.1002/zaac.19673510108.
- [59] N. Fairley, V. Fernandez, M. Richard-Plouet, C. Guillot-Deudon, J. Walton, E. Smith, D. Flahaut, M. Greiner, M. Biesinger, S. Tougaard, D. Morgan, J. Baltrusaitis, Systematic and collaborative approach to problem solving using X-ray photoelectron spectroscopy, Applied Surface Science Advances. 5 (2021) 100112. https://doi.org/10.1016/j.apsadv.2021.100112.

- [60] B.S. Greensfelder, H.H. Voge, G.M. Good, Catalytic and Thermal Cracking of Pure Hydrocarbons: Mechanisms of Reaction, Ind. Eng. Chem. 41 (1949) 2573–2584. https://doi.org/10.1021/ie50479a043.
- [61] K.M. Sundaram, G.F. Froment, Modeling of thermal cracking kinetics—I, Chemical Engineering Science. 32 (1977) 601–608. https://doi.org/10.1016/0009-2509(77)80225-X.
- [62] K.M. Sundaram, P.S. Van Damme, G.F. Froment, Coke deposition in the thermal cracking of ethane, AIChE J. 27 (1981) 946–951. https://doi.org/10.1002/aic.690270610.
- [63] M. Rydén, D. Jing, M. Källén, H. Leion, A. Lyngfelt, T. Mattisson, CuO-Based Oxygen-Carrier Particles for Chemical-Looping with Oxygen Uncoupling Experiments in Batch Reactor and in Continuous Operation, Ind. Eng. Chem. Res. 53 (2014) 6255–6267. https://doi.org/10.1021/ie4039983.
- [64] C. Zheng, J. Cao, Y. Zhang, H. Zhao, Insight into the Oxidation Mechanism of a Cu-Based Oxygen Carrier (Cu → Cu₂ O → CuO) in Chemical Looping Combustion, Energy Fuels. 34 (2020) 8718–8725. https://doi.org/10.1021/acs.energyfuels.0c00941.
- [65] K. Wang, Q. Yu, T. Wu, M. van Sint Annaland, Q. Qin, Thermodynamic and kinetic characteristics of a Cu-Mn composite oxygen carrier for low-temperature chemical-looping air separation, Chemical Engineering Journal. 393 (2020) 124792. https://doi.org/10.1016/j.cej.2020.124792.